Journal of Rock Mechanics and Geotechnical Engineering 15 (2023) 309–322

Contents lists available at ScienceDirect

Journal of Rock Mechanics and Geotechnical Engineering

journal homepage: www.jrmge.cn

Full Length Article

Effect of shear-induced contact area and aperture variations on nonlinear flow behaviors in fractal rock fractures

Changsheng Wang [a,b], Richeng Liu [c], Yujing Jiang [b,d,*], Gang Wang [a], Hengjie Luan [b]

[a] Shandong Key Laboratory of Civil Engineering Disaster Prevention and Mitigation, Shandong University of Science and Technology, Qingdao, 266590, China
[b] State Key Laboratory of Mining Disaster Prevention and Control Co-founded By Shandong Province and the Ministry of Science and Technology, Shandong University of Science and Technology, Qingdao, 266590, China
[c] State Key Laboratory for Geomechanics and Deep Underground Engineering, China University of Mining and Technology, Xuzhou, 221116, China
[d] School of Engineering, Nagasaki University, Nagasaki, 852-8521, Japan

ARTICLE INFO

Article history:
Received 4 January 2022
Received in revised form
17 March 2022
Accepted 14 April 2022
Available online 30 May 2022

Keywords:
Fracture
Shear displacement
Fractal dimension
Nonlinear flow
Contact area
Flow visualization

ABSTRACT

This study experimentally analyzes the nonlinear flow characteristics and channelization of fluid through rough-walled fractures during the shear process using a shear-flow-visualization apparatus. A series of fluid flow and visualization tests is performed on four transparent fracture specimens with various shear displacements of 1 mm, 3 mm, 5 mm, 7 mm and 10 mm under a normal stress of 0.5 MPa. Four granite fractures with different roughnesses are selected and quantified using variogram fractal dimensions. The obtained results show that the critical Reynolds number tends to increase with increasing shear displacement but decrease with increasing roughness of fracture surface. The flow paths are more tortuous at the beginning of shear because of the wide distribution of small contact spots. As the shear displacement continues to increase, preferential flow paths are more distinctly observed due to the decrease in the number of contact spots caused by shear dilation; yet the area of single contacts increases. Based on the experimental results, an empirical mathematical equation is proposed to quantify the critical Reynolds number using the contact area ratio and fractal dimension.

1. Introduction

As a weak plane in rock masses, rock fractures play a vital role in determining the overall hydraulic properties of rock masses. Therefore, substantial efforts have been made to investigate the fluid flow behavior of rock fractures, since a better understanding will definitely assist in the design of many transport engineering activities, such as oil or gas production, thermal energy extraction, and CO_2 sequestration (Mazumder et al., 2006; Schmittbuhl et al., 2008; Neuville et al., 2010; Leung and Zimmerman, 2012; Ju et al., 2013; Feng et al., 2022).

Generally, the fracture model is assumed to be a smooth parallel-plate model, and the fluid flow rate has a linear relationship with the pressure drop, which is called the cubic law (Brown, 1987; Olsson and Barton, 2001; Brush and Thomson, 2003). However, the cubic law is not always accurate in describing the flow characteristics in natural fractures due to the lack of consideration of surface roughness and contact conditions (Zhou et al., 2015; Rong et al., 2016). According to Zimmerman and Bodvarsson (1996), roughness and contact area induce inhomogeneous distribution of fracture aperture, which can cause flow path tortuosity, resulting in occurrence of nonlinear flow even when the value of Reynolds number (Re) is small. Hence, the validity of the cubic law has been challenged, and many scholars have studied nonlinear laminar flow behaviors in fractures (Javadi et al., 2010; Zhang and Nemcik, 2013; Chen et al., 2015; Zou et al., 2015). The critical Reynolds number (Re_c) is commonly defined to quantify the flow transition from linear to nonlinear. A wide range of Re_c (0.001–2300) has been suggested for fluid flow in fractures (Wittke, 1990; Zimmerman et al., 2004; Ranjith and Darlington, 2007; Javadi et al., 2010; Chen et al., 2015; Rong et al., 2017).

Nonlinear flow is affected by many factors, such as normal stress (Zhang and Nemcik, 2013; Xiong et al., 2018), roughness of fracture surface (Javadi et al., 2010; Wang et al., 2016), shear displacement (Javadi et al., 2014; Rong et al., 2016; Yin et al.,

* Corresponding author. State Key Laboratory of Mining Disaster Prevention and Control Co-founded by Shandong Province and the Ministry of Science and Technology, Shandong University of Science and Technology, Qingdao, 266590, China.
E-mail address: jiang@nagasaki-u.ac.jp (Y. Jiang).

Peer review under responsibility of Institute of Rock and Soil Mechanics, Chinese Academy of Sciences.

https://doi.org/10.1016/j.jrmge.2022.04.014

2017; Wang et al., 2020a), and fracture intersection (Kosakowski and Berkowitz, 1999; Liu et al., 2016). Shear displacement is considered to be the most important factor because it can significantly alter the fracture's contact condition, void space geometry, and thereby aperture distribution. Therefore, many efforts have recently been devoted to investigating the influence of shearing on the nonlinear flow behaviors of fractures, including experimental studies and numerical investigations. Javadi et al. (2014) conducted shear-flow tests to study the impact of shearing on nonlinear flow behavior of granite fractures. They found that Re_c showed a trend of increasing with shear displacement. Similar tendency were also observed by Rong et al. (2016) and Wang et al. (2020b). However, opposite results were obtained in the numerical tests. Zhou et al. (2018) established a series of two-dimensional (2D) sheared fracture models by solving the Navier–Stokes (NS) equations, and found that the shear process can enhance the flow nonlinearity. Due to the difficulty of 2D models in exploring the evolution of contact spots during shearing, the impact of shear on nonlinear flow in three-dimensional (3D) fractures has been studied by Zou et al. (2017). It was found that shear-induced aperture and contact spot variations caused complicated channeling and eddy flow, resulting in a significant enhancement of nonlinearity. We speculated that the simulation results deviate from the experimental observations are primarily because the numerical models concerning the shear-induced evolutions of contact area and channelization characteristics lack support from experimental observations.

To better understand the fluid flow through fractures, visualization techniques have been employed in laboratory (Auradou, 2009; Babadagli et al., 2015; Raimbay et al., 2017; Kim et al., 2018). Numerous researches focused on the influence of normal load on the path distribution of inhomogeneous flow and contact condition; however, the effects of shear stress and shear displacement received little attention. Recently, Li et al. (2019) proposed a visualization method to observe the evolution of the channelization of dyed water through rock fractures during shearing using a shear-flow-visualization apparatus. However, the impact of the fracture roughness on fluid flow behavior was not clearly presented. Furthermore, the shear-induced evolutions of the contact area and aperture field affecting the nonlinear flow have not been elucidated. Therefore, visualization techniques are especially needed to clarify whether the shear process affects the flow nonlinearity in fractures.

This paper aims to investigate the impacts of contact area, aperture induced by shear, and roughness of fracture surface, on the flow nonlinearity in fractal fractures. A series of shear-flow-visualization tests was performed on four granite fractures with an extensive range of joint roughness coefficient (JRC). The evolution of aperture, and contact areas of fracture during the shear process and its influences on nonlinear flow behaviors were discussed.

2. Specimen preparation and fracture surface characterization

2.1. Specimen preparation

Granite fractures were used to prepare transparent replicas. Four intact granite blocks (length × width × height = 200 mm × 200 mm × 100 mm) were used to create artificial tensile fractures, and scanned by a 3D laser scanner (Fig. 1). To direct observe the fluid flow behavior, acrylic material was used as the upper part of the specimen, and the plaster material was selected as the lower part. The process of the test sample preparation is shown in Fig. 2. The lower part of the specimen was formed by mixing the plaster, water, and retardant at a mass ratio of 1:0.2:0.005. Then, a plaster replica was taken as the module to manufacture the transparent part. Referring to Li et al. (2019), the transparent specimen was manufactured by a mixture of the main acrylic and hardening agents at a mass ratio of 10:1, which has a fairly close value of unconfined compressive strength to that of the plaster specimen (38.5 MPa).

2.2. Fracture surface measurement

The surfaces were scanned by a 3D laser scanner and their topographical data were obtained (Li et al., 2008). In this study, the scanning interval in both the x- and y-axis was 0.5 mm. For each fracture surface, a scanning dataset consisting of 200 × 400 data points was obtained. The collected topographical data were stored and converted to point clouds, which were used to reconstruct digital rough fracture surfaces (Fig. 1).

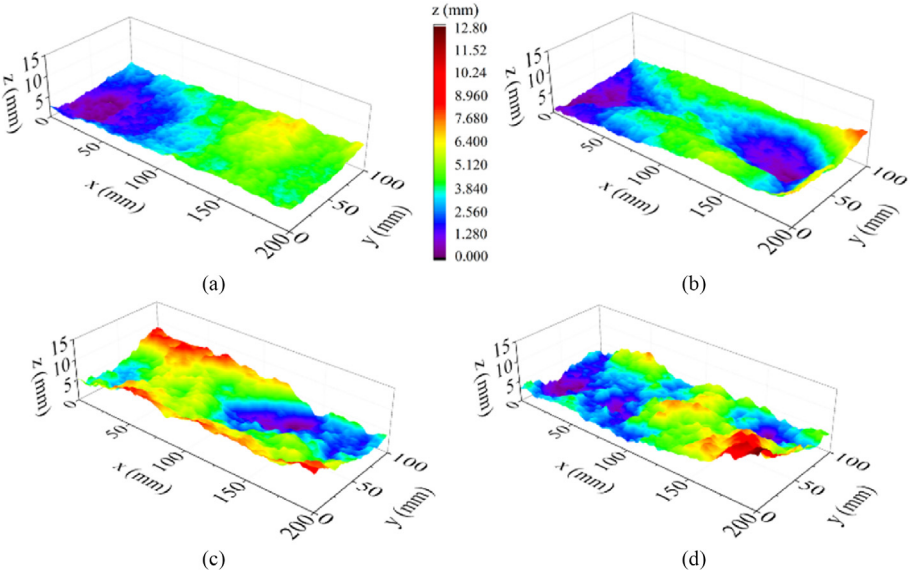

Fig. 1. Digital fracture surfaces with different roughnesses: (a) Fracture G1, (b) Fracture G2, (c) Fracture G3, and (d) Fracture G4.

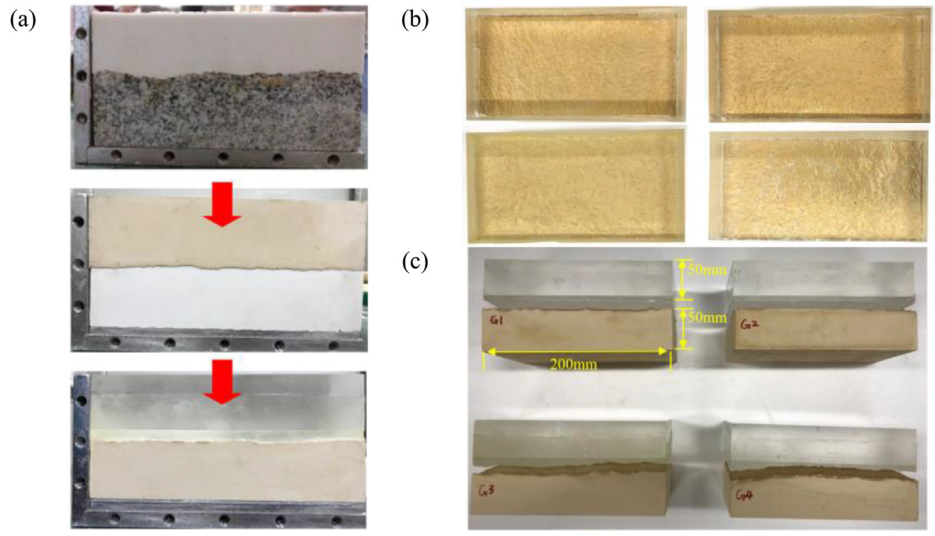

Fig. 2. Fracture specimen preparation: (a) The manufacturing process of transparent specimen, and (b) Top and (c) Side views of the fracture specimens.

The roughness of fracture surface is considered as an essential parameter in qualifying the fluid flow through the fractures, especially when the nonlinear flow occurs due to the local changes in geometries along the flow channels that can induce non-negligible inertial losses. According to the point clouds of rough joint surfaces, the roughness of the surfaces is described by the JRC proposed by Tse and Cruden (1979) as

$$Z_2 = \left[\frac{1}{(n-1)(\Delta x)^2}\sum_{i=1}^{n-1}(z_{i+1}-z_i)^2\right]^{1/2} \quad (1)$$

$$JRC = 32.2 + 32.47\log_{10}Z_2 \quad (2)$$

where Z_2 is the root mean square slope of the profiles, n is the number of data points along the length, z_i is the asperity elevation at point i, and Δx is the interval of the scanning point. Table 1 shows the calculated JRC of the four fracture surfaces, which are labeled G1, G2, G3 and G4. In addition, 2D statistical parameters were introduced to determine the roughness of fracture surface, including the peak asperity height R_p, root mean square of roughness R_{rms} and average roughness R_a. The calculation formulae (Chen et al., 2015; Zhou et al., 2015) can be written as

$$R_p = \max|z_i - z_a| \quad (3)$$

$$R_{rms} = \sqrt{\frac{1}{n}\sum_{i=1}^{n}(z_i - z_a)^2} \quad (4)$$

$$R_a = \frac{1}{n}\sum_{i=1}^{n}(z_i - z_a) \quad (5)$$

where z_a is the height of the mean elevation plane. Table 1 shows the calculated statistical parameters. The obtained results show that R_p ranges from 3.379 mm to 8.711 mm for all fracture surfaces, and R_{rms} and R_a increase with increasing JRC.

Table 1
Topographical parameters of rock fractures.

Fracture No.	Fracture surface description	R_p (mm)	R_{rms} (mm)	R_a (mm)	JRC	D_{va}
G1	Smooth and flat	3.379	1.454	1.195	3.21	1.229
G2	Smooth with major asperities	5.101	1.553	1.306	5.62	1.29
G3	Rough with no major asperities	4.519	1.919	1.606	7.36	1.324
G4	Rough with major asperities	8.711	2.178	1.728	12.16	1.386

2.3. Determination of fractal dimension

Previous studies have shown that the fractal dimension is a suitable parameter for quantifying the roughness of rock surfaces (Mandelbrot and Wheeler, 1983; Huang et al., 1992; Kulatilake et al., 2006; Babadagli et al., 2015; Li and Huang, 2015). Mark and Aronson (1984) pointed out that the morphology of the fracture surface was self-affine, and the fractal dimension can be evaluated by the variogram analysis (VA). Many researchers have adopted the VA method to analyze the relationship between flow behavior and roughness of fracture surface. Raimbay et al. (2017) conducted visualization and hydraulic tests to evaluate the relation between the roughness and permeability. The results showed that the permeability was decreased with increasing variogram fractal dimension. Wang et al. (2016) and Xiong et al. (2018) used the variogram fractal dimension to quantify the roughness of fracture surface and found that a rougher fracture surface could significantly enhance complicated flow regimes, such as eddies and/or backflow. Therefore, in this study, we employed the VA method to investigate the fractal characteristics of rough fracture surfaces.

The variogram function (Mark and Aronson, 1984; Develi and Babadagli, 1998, 2015) can be written as

$$\gamma(h) = \frac{1}{2n}[V(x_i) - V(x_{i+h})]^2 \quad (6)$$

where $\gamma(h)$ is the variogram at lag distance h, n is the number of pairs at a lag distance, and $V(x_i)$ is the sample value at location x_i.

The fractal dimension is expressed from the slope of a log-log plot $\gamma(h)$ and h, written as

$$\gamma(h) = \gamma_0 h^{2H} \tag{7}$$

where γ_0 is a proportionality constant, and H is defined as the Hurst exponent. The range of H is 0–1. The fractal dimension of the fracture surface can be calculated by $D_{va} = 2 - H$.

We applied the VA method to calculating the H value of each profile (cutting line) in the shear direction (y-direction). A total of 200 profiles in the y-direction extracted from each fracture surface were calculated, as shown in Fig. 3. The range of H value varies from 0.425 to 0.848, which is similar to that obtained by Boffa et al. (1998) and Develi and Babadagli (1998). The measured D_{va} of G1, G2, G3 and G4 were 1.229, 1.290, 1.324 and 1.386, respectively (Table 1). A larger value of D_{va} means a rougher surface of a fracture.

3. Experimental methods

3.1. Experimental apparatus

To perform the visualized shear-flow test, a laboratory shear-flow-visualization apparatus at Nagasaki University was adopted (Fig. 4). The apparatus consists of a shear-flow box, control and data

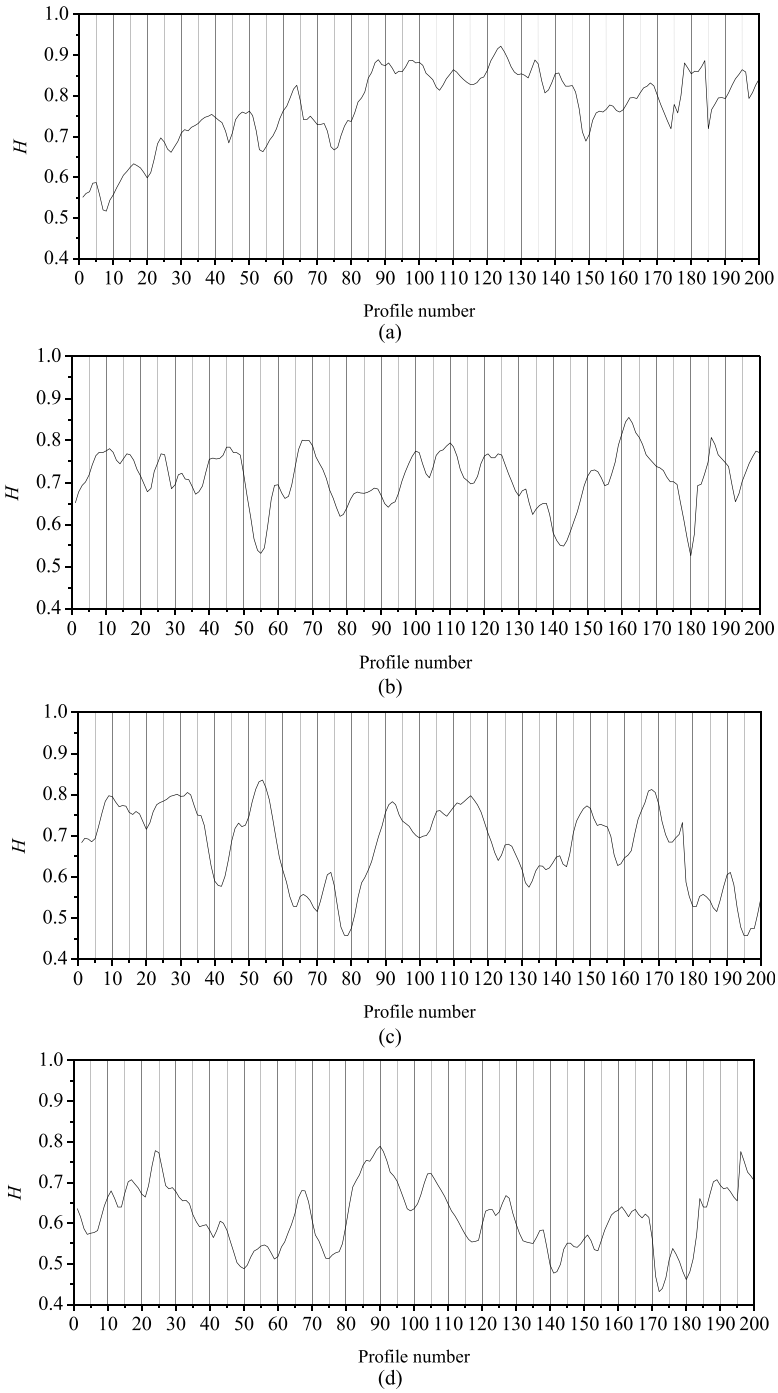

Fig. 3. Hurst exponent (H) of the profiles in the four fractures: (a) Fracture G1, (b) Fracture G2, (c) Fracture G3, and (d) Fracture G4.

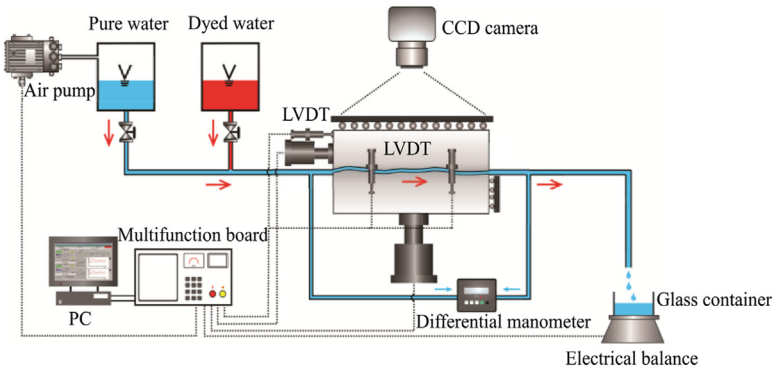

Fig. 4. Schematic diagram of the experimental apparatus. CCD is short for the charge-coupled device. LVDT is short for the linear variable differential transformer. PC means the personal computer.

acquisition system, and vertical and horizontal actuators, which are servo-controlled to apply normal and shear forces with a capacity of 200 kN. The constant inlet water pressure through the rock fracture was supplied by an air pump. The pressure drop was monitored using a differential pressure transducer (model PD-100GA) at a precision of 0.01 kPa. Two sides of boundaries were sealed using pressured soft and elastic gel sheets. For visualization purpose, a window was slotted at the top of the specimen, and a camera was set above to observe the details of fluid flow.

3.2. Experimental procedure

The transparent specimen was placed in the shear-flow-box prior to the tests, and then a constant normal stress of 0.5 MPa was applied to the box through a vertical actuator. The lower box was kept stationary during shearing, while the upper box was sheared up to 10 mm at a rate of 0.5 mm/min. The fluid flow and visualization tests were performed at various shear displacements (d) of 1 mm, 3 mm, 5 mm, 7 mm and 10 mm. Before shearing, a given water pressure was first applied to the inlet of the specimen, and the pressure was maintained for 600 s to ensure that the plaster was absorbed and saturated by water. At each d, 7–10 flow tests with constant water pressures were carried out. The water flowing from the outlet was collected through glassware, and the variation in weight was recorded by an electrical balance with an accuracy of 0.01 g. During each flow test, the constant water pressure was maintained for 200 s to ensure a constant flow rate. After hydraulic tests, visualization tests were conducted at each d under a constant water head (10 cm). To facilitate visualization, we used dyed water to enhance the visibility of the flow paths. The dyed water can be discharged from the fracture by pure water. A high-resolution CCD camera was employed to record the fluid flow images in real time at a rate of one image per second, and recording continued until the pressure drop reached a stable value. This means that the fracture was fully filled with red-dyed water.

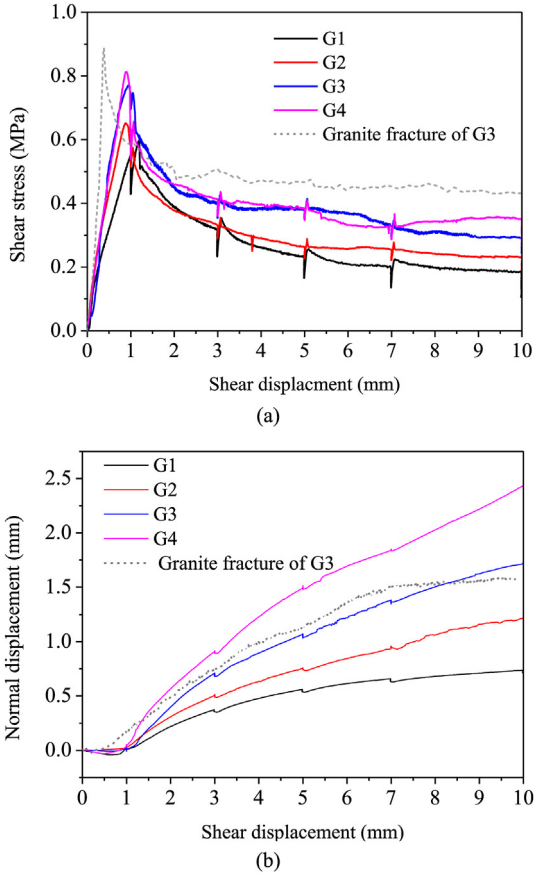

Fig. 5. Mechanical behaviors of fractures in shear-flow tests: (a) Evolution of shear stress with the shear displacement, and (b) Evolution of normal displacement with the shear displacement.

4. Results and discussion

4.1. Shear behaviors

The comparison tests of shear behaviors between the transparent specimen and granite specimen of Fracture G3 were conducted under a normal stress of 0.5 MPa, as shown in Fig. 5. Both cases of shear stress experience a quick rise until the peak, after which stress softening occurs and the stress gradually decreases to an asymptotic value. Compared with the full-granite fracture, the peak shear stress of the transparent fracture is lower, but the peak shear displacement is greater. This difference occurs because the granite is a brittle material, and the strength of granite is larger than that of acrylic and plaster. Despite these differences, the dilation of the transparent specimen was observed to be fairly close to that of the granite fracture because no distinct gouge materials are generated during shearing under lower normal stress conditions. Because the visualization test mainly focuses on the observation of the channelization characteristics of fractures during shearing, which are mainly controlled by the shear dilation-induced aperture variation, the transparent specimen is considered an acceptable specimen for investigating the fluid flow behaviors of fractures.

The variations in shear stress during shear tests for the four fracture specimens G1, G2, G3 and G4 are shown in Fig. 5a. For all cases, the

shear strength abruptly increases to the peak at the initial shear stage. The peak shear stresses for G1, G2, G3 and G4 are 0.554 MPa, 0.652 MPa, 0.771 MPa and 0.813 MPa, respectively, and the corresponding peak shear displacement d_p ranges from 0.813 mm to 1.003 mm. Then, the shear strength reduction occurs, and the stress gradually decreases to an asymptotic value, which represents residual shear strength at the steady shearing stage. The residual shear stresses are 0.184 MPa, 0.244 MPa, 0.292 MPa and 0.351 MPa, respectively. Moreover, there is an obvious influence of roughness on the shear behaviors, where rougher fractures exhibit higher values of peak and residual shear stresses. This is because the rougher fractures exhibit larger high-order asperities, and a larger shear stress is needed to shear the specimen, resulting in larger peak and residual shear stresses.

The variations in the normal displacement with different fractures are plotted in Fig. 5b. The normal displacement during shearing exhibits nonlinear descending-ascending behavior. The normal displacement slightly decreases at first due to the asperity and surface interlocking, after which dilation occurs and the deformation gradually increases. The ultimate normal displacement (corresponding to d of 10 mm), d_u, ranges from 0.735 mm to 2.426 mm, and the rougher fractures display a larger value of d_u.

4.2. Nonlinear flow behavior

For viscous flow, the cubic law is applicable to describing the laminar flow in fractures (Konzuk and Kueper, 2004; Tzelepis et al., 2015), written as

$$Q = -\frac{we_h^3}{12\mu}\frac{\Delta P}{L} \tag{8}$$

where Q is the flow rate, which is obtained by calculating the weight of water per unit time; w is the fracture width; e_h is the hydraulic aperture; ΔP is the pressure drop in the flow direction; μ is the viscosity of the fluid; and L is the fracture length. Note the pressure gradient (∇P) is defined as $\nabla P = \Delta P/L$.

By increasing Q, the flow behavior deviating from the linear flow regime can be observed. Forchheimer's law is commonly employed to describe nonlinear flow behavior in rock fractures (Zimmerman et al., 2004; Zhang and Nemcik, 2013), which can be written as

$$-\nabla P = aQ + bQ^2 \tag{9}$$

$$a = \frac{\mu}{T_0} = \frac{12\mu}{we_h^3} \quad b = \frac{\alpha\rho}{w^2 e_h^2} \tag{10}$$

where a and b are the linear and nonlinear coefficients, respectively; and α represents the non-Darcy coefficient.

Zeng and Grigg (2006) introduced the coefficient E to describe the flow regime transition, written as

$$E = \frac{bQ^2}{aQ + bQ^2} \tag{11}$$

Zeng and Grigg (2006) suggested that the onset of nonlinear flow behavior occurs when $E = 0.1$. The corresponding Reynolds number (Re) is the critical Reynolds number (Re_c), written as

$$Re = \frac{\rho Q}{\mu w} \tag{12}$$

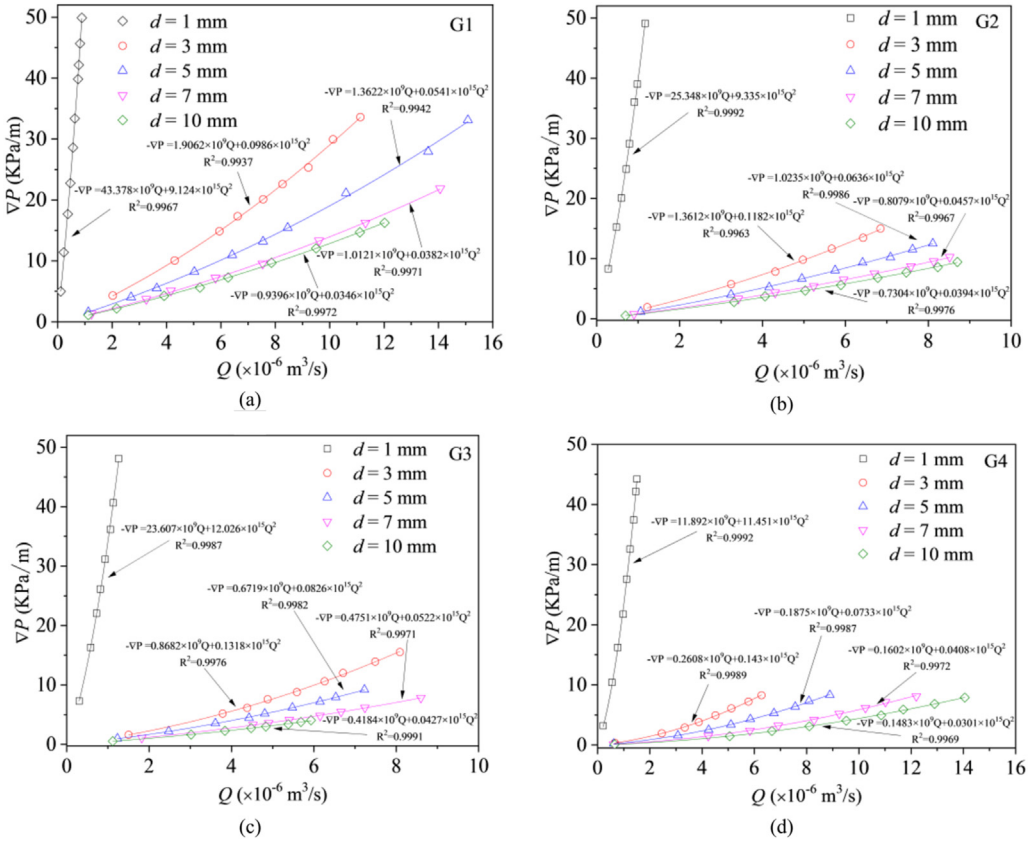

Fig. 6. Regression analysis of pressure drop as a function of measured flow rate using Forchheimer's law for different fractures: (a) Fracture G1, (b) Fracture G2, (c) Fracture G3, and (d) Fracture G4.

Table 2
Calculated results of a and b for different fractures during shear process.

d (mm)	G1		G2		G3		G4	
	a (10^9 kg s^{-1} m^{-5})	b (10^{15} kg m^{-8})	a (10^9 kg s^{-1} m^{-5})	b (10^{15} kg m^{-8})	a (10^9 kg s^{-1} m^{-5})	b (10^{15} kg m^{-8})	a (10^9 kg s^{-1} m^{-5})	b (10^{15} kg m^{-8})
1	43.378	9.124	25.348	9.335	23.607	12.026	11.892	11.451
3	1.9062	0.0986	1.3612	0.1182	0.8682	0.1318	0.2608	0.143
5	1.3622	0.0541	1.0235	0.0636	0.6719	0.0826	0.1875	0.0733
7	1.0121	0.0382	0.8079	0.0457	0.4751	0.0522	0.1602	0.0408
10	0.9396	0.0346	0.7304	0.0394	0.4184	0.0427	0.1483	0.0301

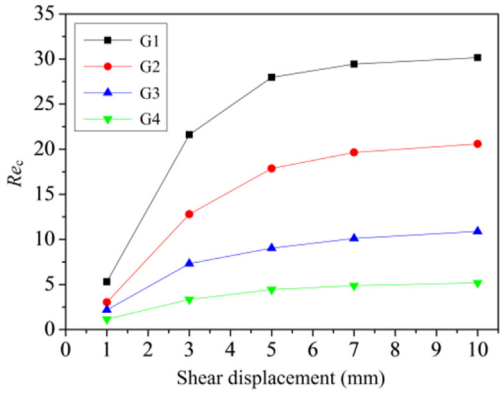

Fig. 7. Evolutions in critical Reynolds number versus shear displacement.

$$Re_c = \frac{aE}{b\mu w(1-E)} \tag{13}$$

Because the fracture was well-matched at the initial shear, the applied water pressure was so small that no water was measured at the shear contraction stage. Therefore, the flow tests were conducted at a shear displacement of 1 mm, where shear dilation occurs. Fig. 6 shows the relationships between ∇P and Q for various fractures under different values of d. The ∇P-Q curves show clear nonlinear characteristics. It is clear that the experimental data can be well fitted by the quadratic polynomial regression of the Forchheimer's law. The shear displacement markedly alters the slope of the curves of the four fractures. When the shear advances, the ∇P-Q curve's slope becomes flatter due to shear dilation. Based on Eq. (9), both a and b for all cases were calculated, as summarized in Table 2. Both a and b decrease with increasing shear displacement.

Based on Eq. (13), Re_c was calculated. The variations in Re_c during shear processes for the four fractures are shown in Fig. 7. The results show that as d increases, Re_c increases and exhibits two different stages for all test cases. Re_c significantly increases as d increases to 3 mm and then gradually increases until reaching a constant value as d exceeds 5 mm. It was also found that the ranges of Re_c are different for the four fractures. The range of Re_c is 3.35–30.17 for Fracture G1, 1.95–20.6 for Fracture G2, 1.57–10.89 for Fracture G3, and 1.15–5.19 for Fracture G4. The rougher fracture surface exhibits a lower value of Re_c. The results of the Re_c–d curves are similar to the findings of Javadi et al. (2014).

4.3. Visualization

Figs. 8–11 display the images of fluid flow evolution in fractures under various shear displacements. It was observed that there is a larger number of connected flow paths at the initial shearing (i.e. $d = 1$ mm). The velocity of dyed water flow over the whole fracture was low, requiring 115 s to fill the void space. The flow resistance is larger at the initial shearing because the two fracture surfaces were slightly mismatched, forming a closed fracture aperture with more contact spots. As d advances, channeling was more distinctly observed. The numbers of flow paths and contact spots decrease due to the shear dilation, and the contact is focused at much fewer locations of larger areas. The velocity of dyed water that fills the aperture is high for a larger value of d due to the reduction of flow resistance caused by shear dilation. Under the same shear displacement, the number of preferential flow paths was larger for a fracture with a smaller value of JRC. This phenomenon is attributed to the contacts mainly focusing on major asperities for rougher fractures. In addition, the effects of the morphological behaviors of fractures on the flow patterns are shown in Figs. 8–11. Because the surface of Fracture G1 is smooth and flat, the number of contact spots is relatively large, and the contact areas are in the form of "islet" (Fig. 8). Similar patterns were also observed for Fracture G3. This occurred because Fracture G3 is rough with no major asperities but has many similar asperities. For Fractures G2 and G4, the existence of major asperities tends to climb each other during shear process. This significantly decreases the contact area, and the contact areas are focused at fewer locations of main height asperities.

4.4. Evolution of the aperture and contact ratio

Based on the fracture surface scanning data, the mechanical aperture of fracture, e_m, can be obtained from (Li et al., 2008):

$$e_m = e_0 - \Delta b_n + \Delta d \tag{14}$$

where e_0 represents the initial mechanical aperture, Δb_n is the change in aperture induced by normal loading and Δd is the change in aperture due to shearing. Δb_n is equal to zero under constant normal load conditions. Δd is the variation in the normal displacement.

Based on Eqs. (8) and (14), e_h and e_m at different shear displacements were calculated. Note that the fractures were perfectly mated, forming a tightly closed fracture, and no water was detected for all fractures before shearing. Therefore, e_0 was assumed to equal zero, and the contact area ratio was assumed to approach 1 (Li et al., 2008). Because the tested specimens have fracture surfaces with different roughnesses, variation in the frequency of the mechanical aperture distributions under different values of d can be obtained, as shown in Fig. 12. According to Huang et al. (2017), negative values of aperture indicate shear-induced contacts. The e_m distributions of the four fractures at different values of d follow Gauss distributions. As the value of d increases, the maximum frequency of e_m decreases, while the mean aperture tends to increase. This occurs because shear dilation causes variations in the fracture geometry and an increase in the fracture distribution. A wider range of the aperture distribution was observed for the relatively rough fracture, indicating that shear-induced fracture aperture distributions become more anisotropic and heterogeneous for rougher fractures. For example, for Fracture G2, which has the roughest surface, the aperture distribution is in the range of 0–5.95 mm at

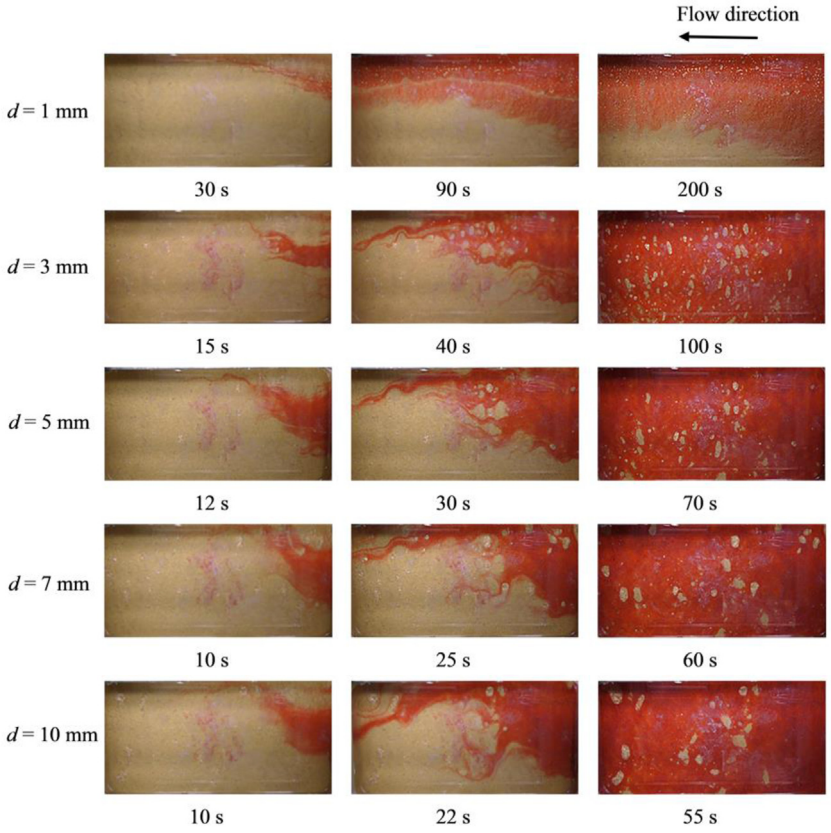

Fig. 8. Evolution of the dyed water flow in Fracture G1 at various shear displacements.

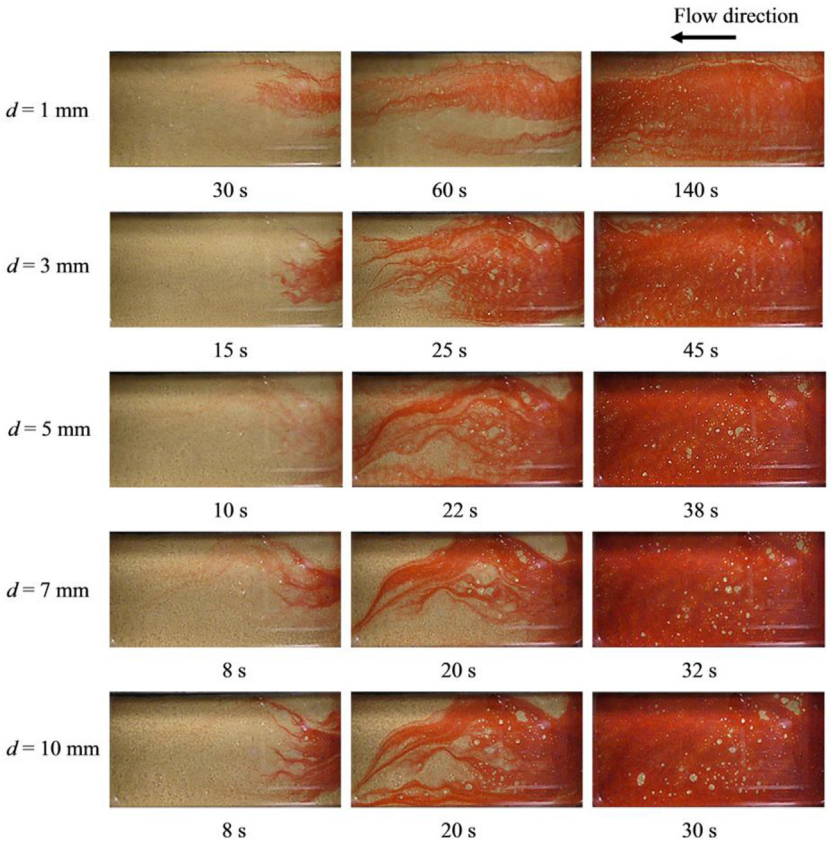

Fig. 9. Evolution of the dyed water flow in Fracture G2 at various shear displacements.

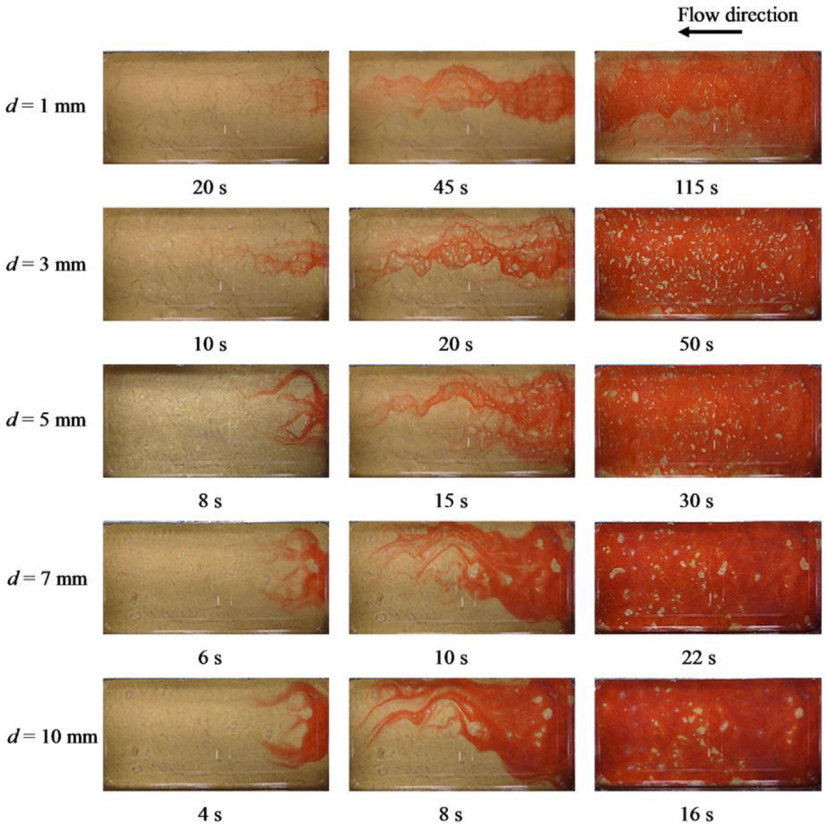

Fig. 10. Evolution of the dyed water flow in Fracture G3 at various shear displacements.

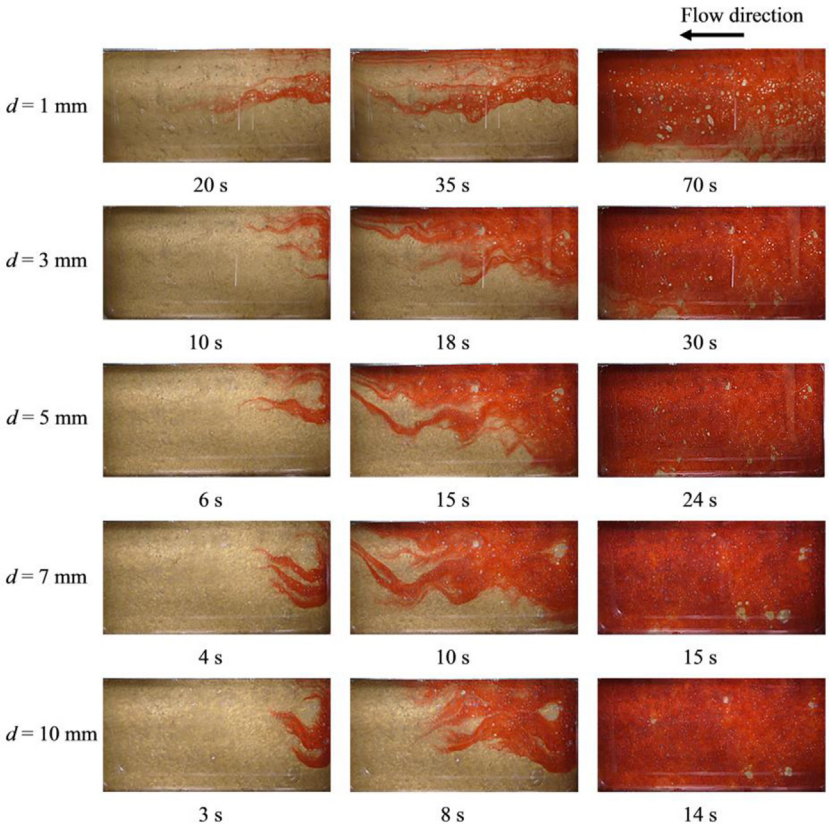

Fig. 11. Evolution of the dyed water flow in Fracture G4 at various shear displacements.

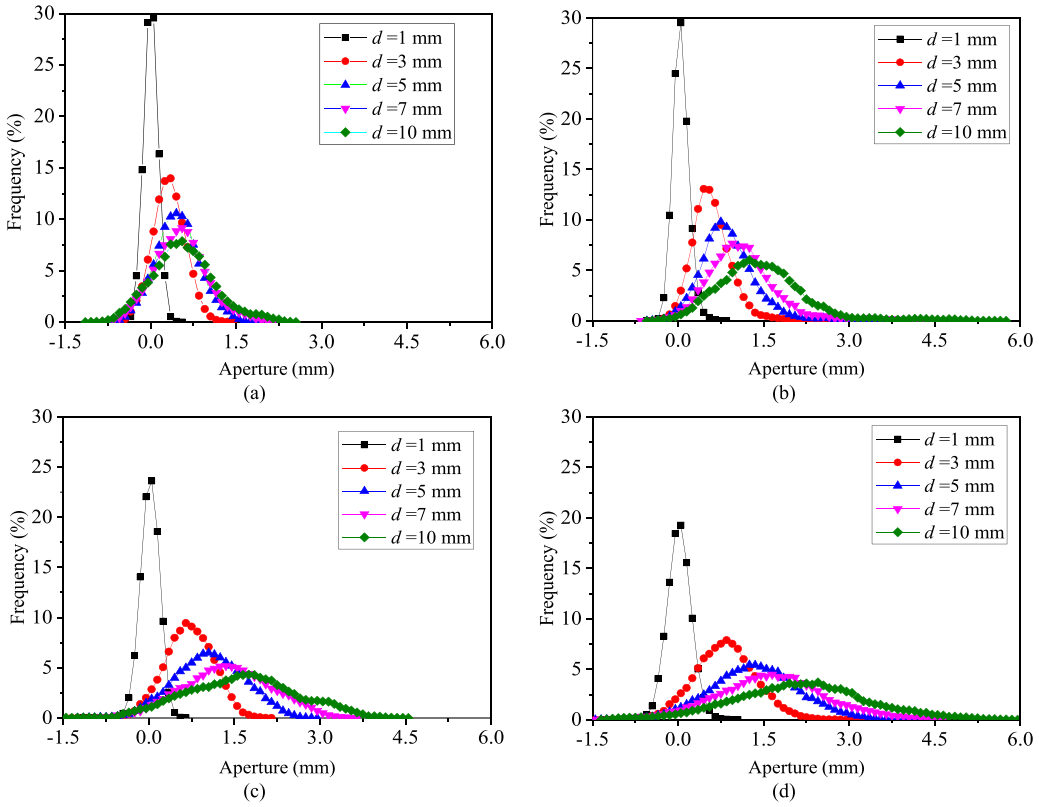

Fig. 12. The aperture-frequency curves during shearing for different fracture surfaces: (a) Fracture G1, (b) Fracture G2, (c) Fracture G3, and (d) Fracture G4. The negative values represent the shear-induced contact areas.

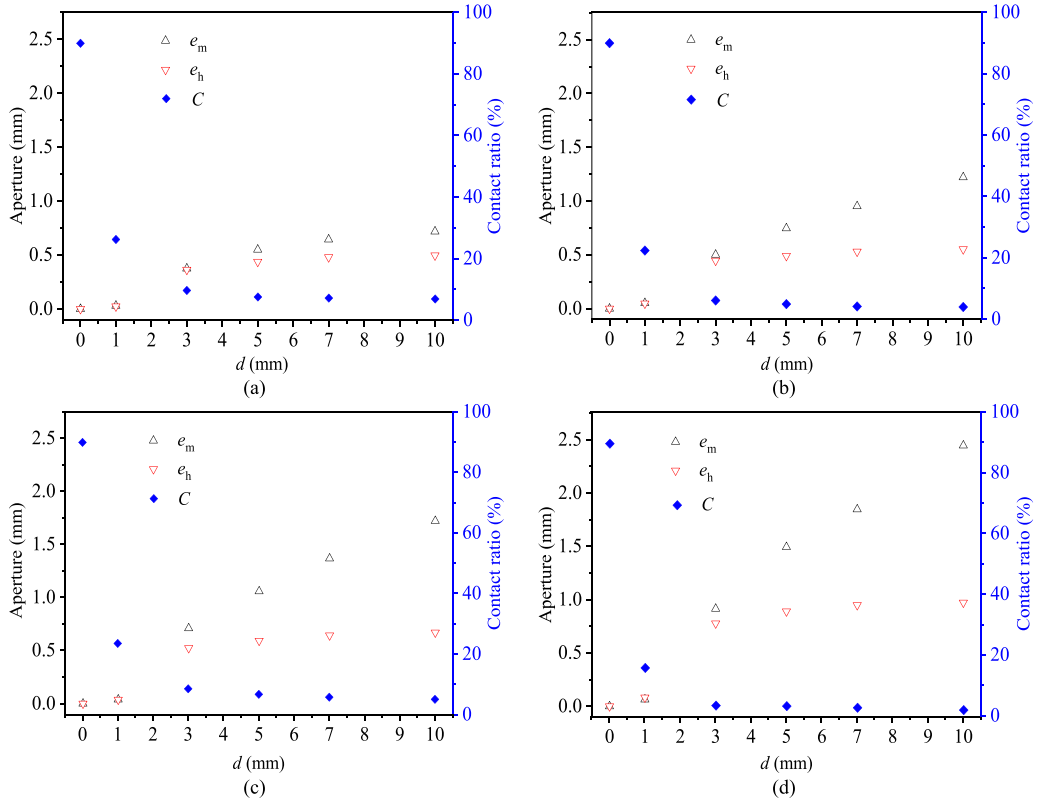

Fig. 13. The evolutions of hydraulic aperture e_h, mechanical aperture e_m and contact ratio C during shearing: (a) Fracture G1, (b) Fracture G2, (c) Fracture G3, and (d) Fracture G4.

$d = 10$ mm, while for Fracture G1, which has the smoothest surface, the aperture distribution is in the range of 0–2.55 mm at $d = 10$ mm. Fig. 13 shows the variations in e_m, e_h and C of Fractures G1-G4 under different values of d. The contact area ratio (C) was measured by the image binary method (Develi and Babadagli, 2015), which is defined by calculating the ratio of contact area to the total area. For all tests, both e_h and e_m significantly increase when d increases from 1 mm to 3 mm due to the rapid growth of shear dilation at this stage. Then, various apertures become steadier for a larger shear displacement due to the gradual reduction of shear dilation. However, the various trends of C are inverse to the change in aperture. The shear dilation-induced C rapidly decreases in the shear displacement range of 1–3 mm and remains at a constant value. It was also observed that the value of e_m is larger than that of e_h, and the difference between e_m and e_h becomes larger with increasing shear displacement. Additionally, a larger deviation between e_m and e_h was observed for rougher fractures due to the stronger nonlinear flow for rougher fractures.

4.5. Discussion

Nonlinear flow behavior is distinctly determined by the inertial effect, which is affected by the roughness, contact conditions, and aperture distribution of fractures. During shearing, the aperture and contact areas vary significantly due to shear dilation, which affects the hydraulic properties of fractures. Based on the visualization results, the two fracture surfaces were slightly mismatched at the initial shear stage, forming a closed aperture with a larger number of contact spots. Under this condition, the flow behavior is easily influenced by the roughness of fractures, and the existing contacts make the flow paths more tortuous; thus, the nonlinearity of fluid flow is strong with a small value of Re_c. With an increase in d, the shear dilation causes the apparent variation in the fracture geometry, and this change will decrease the relative roughness, contact conditions and flow tortuosity, leading to remarkable decreases in both a and b. Meanwhile, the roughness of the fracture surface has a limited impact on the nonlinear flow. Based on Eq. (10), the variation in the value of a is dependent on the aperture, and shear dilation can cause a decrease in the value of a. Similarly, b is related to the aperture and non-Darcy coefficient α. An increase in aperture and/or decrease in flow tortuosity leads to a decrease in the value of b. According to Eq. (13), Re_c is related to the ratio of a to b. The reduction degree of a is smaller than that of b during the shear process, which leads to an increase in Re_c. In addition, as shown in Fig. 7, the rougher fracture can significantly increase the flow nonlinearity with a lower value of Re_c. For rough-walled fractures, the complex morphology of the surface, contacts or sharp changes in fracture wavelength is the reason for inertial losses that cause the flow regimes to deviate from linearity. Additionally, during shearing, shear-induced fracture aperture distributions become more anisotropic and heterogeneous with increased roughness of fracture surface (Fig. 12). These features tend to increase inertial losses and result in a lower value of Re_c.

4.6. Critical conditions for nonlinear flow

The normalized transmissivity (T/T_0), which is the ratio of the apparent transmissivity (T) at a certain flow rate to the transmissivity (T_0) at a significantly small flow rate, has been commonly used to describe the nonlinear flow behavior in fractures (Zimmerman et al., 2004).

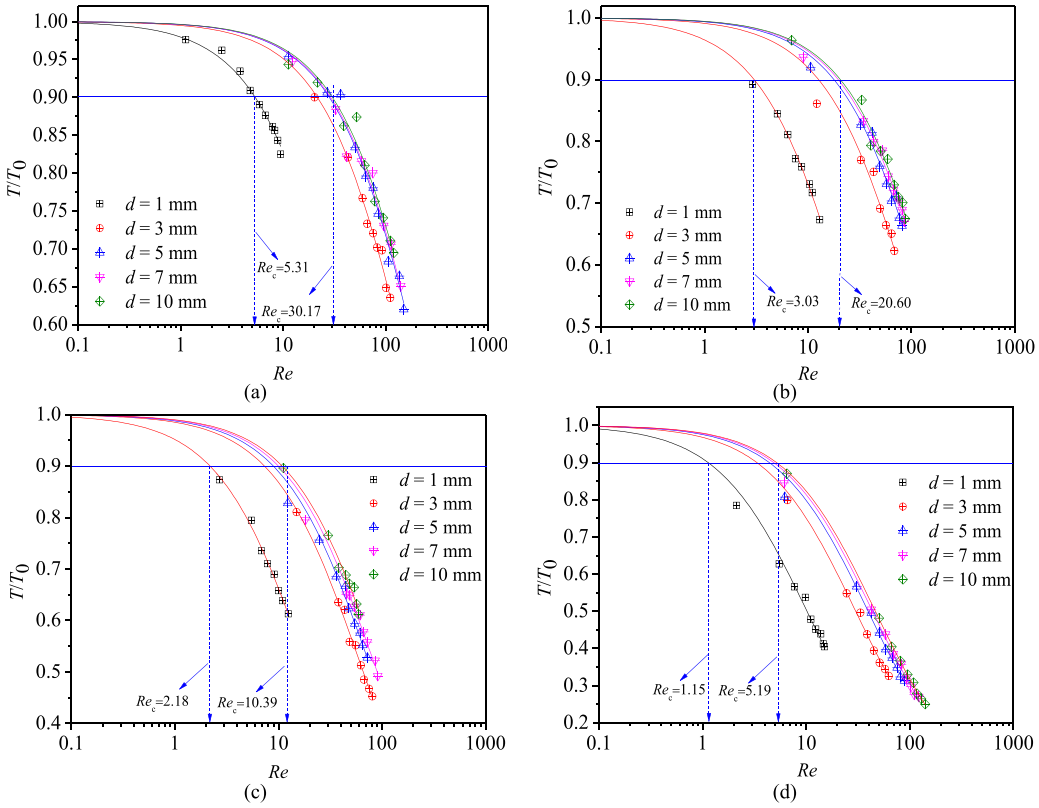

Fig. 14. Relationships between normalized transmissivity (T/T_0) and Reynolds number (Re) for (a) Fracture G1, (b) Fracture G2, (c) Fracture G3, and (d) Fracture G4.

$$\frac{T}{T_0} = \frac{1}{1+\beta Re} \tag{15}$$

where $T_0 = \mu/a$ and β is the Forchheimer coefficient.

According to Yu et al. (2017), $T/T_0 = 0.9$ means that 10% of the total pressure was induced by nonlinearity, which equals $E = 0.1$. Therefore, Eq. (15) can be expressed as

$$\frac{T}{T_0} = \frac{-\mu Q \Big/ w\left(aQ + bQ^2\right)}{-\mu Q/w(aQ)} = 1 - E \tag{16}$$

Hence, the expression of Re_c can also be written as

$$Re_c = \frac{E}{1-E}\frac{1}{\beta} \tag{17}$$

Fig. 14 plots the T/T_0–Re curves of four rough fractures. The experimental data fit well with the prediction by Eq. (17). For all cases, T/T_0 decreases with increasing value of Re. At small value of Re, T/T_0 is approximately equal to 1. As Re reaches a critical value, T/T_0 sharply decreases because of the inertia effect. Additionally, the T/T_0–Re curves gradually shift upward with increasing d. The T/T_0–Re curve shifts more significantly in the d range of 1–3 mm than in the range of 3–10 mm, indicating that the nonlinearity of fluid flow is stronger at low values of d.

Previous studies have reported that β can be influenced by special circumstances (Wang et al., 2016, 2020b; Yin et al., 2017). Wang et al. (2016) found that the value of β is increased by approximately one order of magnitude as the fractal dimension increases from 2.2 to 2.5. Yin et al. (2017) observed that the decline in the value of β decreases with increasing value of d, but increases with the applied normal load. To further analyze the impact of contacts and roughness on the value of β, the variations in β under different values of d were calculated by Eq. (15). Fig. 15 shows the relationship between β and C. The plots suggest that a power function can well describe the relationship for each fracture. The larger value of D_{va} has a steeper slope, indicating that the value of β is significantly affected by the contact area ratio for a rougher fracture. Fig. 16 shows the β–D_{va} curves of fractures under different shear displacements, showing that $\log_{10}\beta$ has a strong linear relation between D_{va} with a similar slope. Motivated by the evolution characteristics of the curves shown in Figs. 15 and 16, an enhanced power-law is presented as

$$\beta = c^n e^{(kD_{va}+d)} \tag{18}$$

where n, k and d represent the regression coefficients. The best fits of β with the variables C and D_{va} are plotted in Fig. 17, which shows

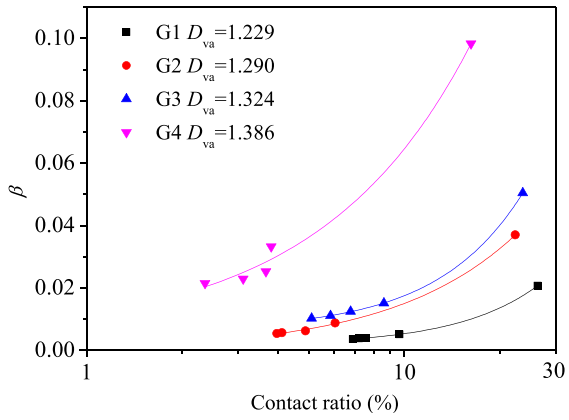

Fig. 15. Relationship between the Forchheimer coefficient β with the contact ratio C.

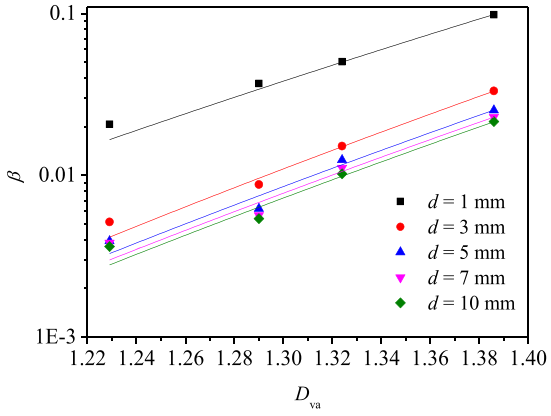

Fig. 16. Relationship between Forchheimer coefficient β and the fractal dimension D_{va} under different shear displacements.

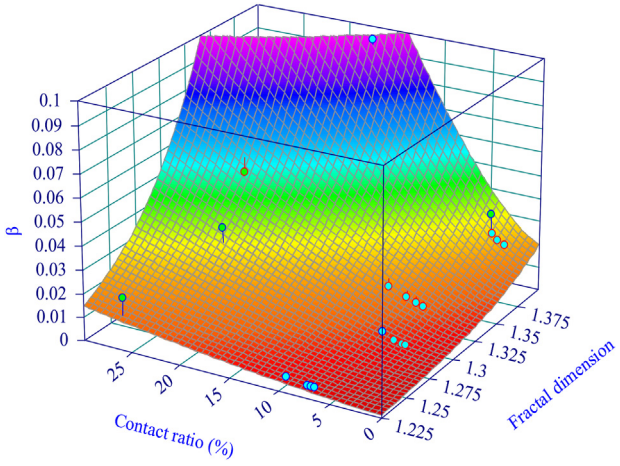

Fig. 17. Regression analysis of Forchheimer coefficient β as a function of the fractal dimension D_{va} and contact ratio C.

a strong relationship. The regression values in Eq. (18) are $n = 0.897$, $k = 15.29$ and $d = -26.01$ with $R^2 = 0.973$. Substituting Eq. (18) into Eq. (17) yields the Re_c as

$$Re_c = \frac{E}{1-E}\frac{1}{C^{0.897}e^{(15.29D_{va}-26.01)}} \tag{19}$$

Eq. (19) supplies a simple mathematical prediction through the contact area ratio and fractal dimension to quantify Re_c for fluid flow in rough fractures. Fig. 18 shows the relationship between Re_c and C. The variation in Re_c was calculated using $E = 0.1$. The predicted values of Re_c ($Re_{c_{calculate}}$) are consistent with the experimental data ($Re_{c_{test}}$). Re_c shows a decreasing trend with increasing values of C and D_{va}. The average estimation errors of Eq. (19) (E_{ave}) can be obtained by

$$E_{ave} = \frac{1}{M}\sum_{i=1}^{M}\left(\frac{Re_{c_{test}} - Re_{c_{calculate}}}{Re_{c_{test}}}\right)^2 \times 100\% \tag{20}$$

where M is the number of conducted tests. The average estimation error calculated by Eq. (20) is 5.71%, which further validate the mathematical prediction model.

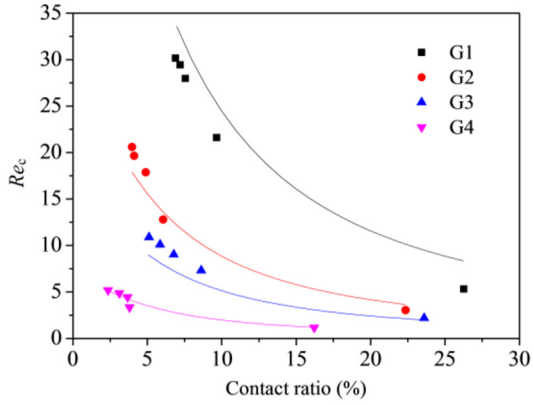

Fig. 18. Predications of critical Reynolds number Re_c as a function of contact ratio C and comparisons with the experimental results.

5. Conclusions

In this work, we conducted shear-flow tests on four transparent replicas of different rough granite fractures using a visualization system of the shear-flow apparatus. Based on this apparatus, a visualization method was developed to determine the channelization behavior of fractures with varying displacements of shear ($d = 1$ mm, 3 mm, 5 mm, 7 mm and 10 mm). The evolution of flow paths, contact conditions and aperture distributions were analyzed to determine how the shear displacement affects the nonlinear flow behavior of fractures with different roughness.

The obtained results show that the relationship between the pressure drop and flow rate is distinctly nonlinear, and can be fitted well by Forchheimer's law. The critical Reynolds number (Re_c) exhibits an ascending trend with increasing shear displacement. The evolution of Re_c can be explained by the results of visualized shear-flow test. When d is small, the tight aperture with many small contact spots causes the flow path to be more tortuous, resulting in a strong nonlinearity of fluid flow. As d continuously advances, the dilation significantly decreases the contact ratio (C), and preferential channels were more characteristically observed, leading to increases in Re_c. A mathematical expression of Re_c based on C and fractal dimension (D_{va}) was proposed, and the experimental results confirm the validity of the mathematical prediction model. The Re_c shows a descending trend with increasing C.

In the present study, we conducted shear-flow tests on rough-walled fractures with a small stress of 0.5 MPa to guarantee that the fracture surface is negligibly damaged and thus, the influence of the production of gouge material on flow characteristics can be ignored. However, the fracture may be subject to various stress levels and boundary conditions, which directly influence the contact condition and fracture aperture field, as well as the fluid flow behavior in fractures. In future work, we will focus on the influence of normal stress and boundary conditions on the fluid flow nonlinearity in fractures during shearing and facilitate predictive models of the nonlinear flow regime by considering the impact of boundary stress. Besides, limited by the test equipment, the CCD camera cannot capture nonlinear flow behaviors, e.g. eddies and backflow. In future studies, new visualization techniques, such as particle image velocimetry, will be adopted to obtain more details on flow, including the distributions of velocity and streamlines, for fractures undergoing different shear displacements.

Declaration of competing interest

The authors declare that they have no known competing financial interests or personal relationships that could have appeared to influence the work reported in this paper.

Acknowledgments

This study has been partially funded by National Key Research and Development Program of China (Grant No. 2020YFA0711800), the National Natural Science Foundation of China (Grant No. 51979272), and the Natural Science Foundation of Shandong Province, China (Grant No. ZR2021QE069). These supports are gratefully acknowledged.

References

Auradou, H., 2009. Influence of wall roughness on the geometrical, mechanical and transport properties of single fractures. J. Phys. D Appl. Phys. 42 (21), 214015.
Babadagli, T., Ren, X., Develi, K., 2015. Effects of fractal surface roughness and lithology on single and multiphase flow in a single fracture: an experimental investigation. Int. J. Multiphas. Flow 68, 40–58.
Boffa, J.M., Allain, C., Hulin, J.P., 1998. Experimental analysis of fracture rugosity in granular and compact rocks. Eur. Phys. J. Appl. Phys. 2 (3), 281–289.
Brown, S.R., 1987. Fluid flow through rock joints: the effect of surface roughness. J. Geophys. Res. Solid Earth 92 (B2), 1337–1347.
Brush, D.J., Thomson, N.R., 2003. Fluid flow in synthetic rough-walled fractures: Navier–Stokes, Stokes, and local cubic law simulations. Water Resour. Res. 39, 1085.
Chen, Y., Zhou, J., Hu, S., Hu, R., Zhou, C., 2015. Evaluation of Forchheimer equation coefficients for non-Darcy flow in deformable rough-walled fractures. J. Hydrol. 529, 993–1006.
Develi, K., Babadagli, T., 1998. Quantification of natural fracture surfaces using fractal geometry. Math. Geol. 30 (8), 971–998.
Develi, K., Babadagli, T., 2015. Experimental and visual analysis of single-phase flow through rough fracture replicas. Int. J. Rock Mech. Min. Sci. 73, 139–155.
Feng, Q., Jin, J., Zhang, S., Liu, W., Yang, X., Li, W., 2022. Study on a damage model and uniaxial compression simulation method of frozen–thawed rock. Rock Mech. Rock Eng. 55, 187–211.
Huang, S., Oelfke, S.M., Speck, R.C., 1992. Applicability of fractal characterization and modelling to rock joint profiles. Int. J. Rock Mech. Min. Sci. Geomech. Abstr. 29 (2), 89–98.
Huang, N., Liu, R., Jiang, Y., 2017. Numerical study of the geometrical and hydraulic characteristics of 3D self-affine rough fractures during shear. J. Nat. Gas Sci. Eng. 45, 127–142.
Javadi, M., Sharifzadeh, M., Shahriar, K., 2010. A new geometrical model for non-linear fluid flow through rough fractures. J. Hydrol. 389 (1–2), 18–30.
Javadi, M., Sharifzadeh, M., Shahriar, K., Mitani, Y., 2014. Critical Reynolds number for nonlinear flow through rough-walled fractures: the role of shear processes. Water Resour. Res. 50 (2), 1789–1804.
Ju, Y., Zhang, Q., Yang, Y., Xie, H., Gao, F., Wang, H., 2013. An experimental investigation on the mechanism of fluid flow through single rough fracture of rock. Sci. China E 56 (8), 2070–2080.
Kim, K.Y., Oh, J., Han, W.S., Park, K.G., Shinn, Y.J., Park, E., 2018. Two-phase flow visualization under reservoir conditions for highly heterogeneous conglomerate rock: a core-scale study for geologic carbon storage. Sci. Rep. 8 (1), 1–10.
Konzuk, J.S., Kueper, B.H., 2004. Evaluation of cubic law based models describing single-phase flow through a rough-walled fracture. Water Resour. Res. 40 (2), 1–17.
Kosakowski, G., Berkowitz, B., 1999. Flow pattern variability in natural fracture intersections. Geophys. Res. Lett. 26 (12), 1765–1768.
Kulatilake, P.H.S.W., Balasingam, P., Park, J., Morgan, R., 2006. Natural rock joint roughness quantification through fractal techniques. Geotech. Geol. Eng. 24 (5), 1181–1202.
Leung, C.T., Zimmerman, R.W., 2012. Estimating the hydraulic conductivity of two-dimensional fracture networks using network geometric properties. Transport Porous Media 93 (3), 777–797.
Li, B., Jiang, Y., Koyama, T., Jing, L., Tanabashi, Y., 2008. Experimental study of the hydro-mechanical behavior of rock joints using a parallel-plate model containing contact areas and artificial fractures. Int. J. Rock Mech. Min. Sci. 45 (3), 362–375.
Li, Y., Huang, R., 2015. Relationship between joint roughness coefficient and fractal dimension of rock fracture surfaces. Int. J. Rock Mech. Min. Sci. 75, 15–22.
Li, B., Liu, R., Jiang, Y., 2019. An experimental method to visualize shear-induced channelization of fluid flow in a rough-walled fracture. Hydrogeol. J. 27 (8), 3097–3106.
Liu, R., Li, B., Jiang, Y., 2016. Critical hydraulic gradient for nonlinear flow through rock fracture networks: the roles of aperture, surface roughness, and number of intersections. Adv. Water Resour. 88, 53–65.
Mandelbrot, Benoit B., Wheeler, John A., 1983. The Fractal Geometry of Nature. W.H. Freeman, New York.
Mark, D.M., Aronson, P.B., 1984. Scale-dependent fractal dimensions of topographic surfaces: an empirical investigation, with applications in geomorphology and computer mapping. Math. Geol. 16 (7), 671–683.
Mazumder, S., Karnik, A.A., Wolf, K.H.A., 2006. Swelling of coal in response to CO2 sequestration for ECBM and its effect on fracture permeability. SPE J. 11 (3), 390–398.

Neuville, A., Toussaint, R., Schmittbuhl, J., 2010. Fracture roughness and thermal exchange: a case study at Soultz-sous-Forêts. C. R. Geosci. 342 (7–8), 616–625.
Olsson, R., Barton, N., 2001. An improved model for hydromechanical coupling during shearing of rock joints. Int. J. Rock Mech. Min. Sci. 38 (3), 317–329.
Raimbay, A., Babadagli, T., Kuru, E., Develi, K., 2017. Fractal analysis of single-phase water and polymer solution flow at high rates in open and horizontally displaced rough fractures. Int. J. Rock Mech. Min. Sci. 92, 54–71.
Ranjith, P.G., Darlington, W., 2007. Nonlinear single-phase flow in real rock joints. Water Resour. Res. 43 (9), 1385–1394.
Rong, G., Yang, J., Cheng, L., Zhou, C., 2016. Laboratory investigation of nonlinear flow characteristics in rough fractures during shear process. J. Hydrol. 541, 1385–1394.
Rong, G., Hou, D., Yang, J., Cheng, L., Zhou, C., 2017. Experimental study of flow characteristics in non-mated rock fractures considering 3D definition of fracture surfaces. Eng. Geol. 220, 152–163.
Schmittbuhl, J., Steyer, A., Jouniaux, L., Toussaint, R., 2008. Fracture morphology and viscous transport. Int. J. Rock Mech. Min. Sci. 45 (3), 422–430.
Tse, R., Cruden, D.M., 1979. Estimating joint roughness coefficients. Int. J. Rock Mech. Min. Sci. Geomech. Abstr. 16 (5), 303–307.
Tzelepis, V., Moutsopoulos, K.N., Papaspyros, J.N., Tsihrintzis, V.A., 2015. Experimental investigation of flow behavior in smooth and rough artificial fractures. J. Hydrol. 521, 108–118.
Wang, M., Chen, Y., Ma, G., Zhou, J., Zhou, C., 2016. Influence of surface roughness on nonlinear flow behaviors in 3D self-affine rough fractures: lattice Boltzmann simulations. Adv. Water Resour. 96, 373–388.
Wang, C., Jiang, Y., Luan, H., Sugimoto, S., 2020a. Effect of shearing on hydraulic properties of rough-walled fractures under different boundary conditions. Energy Sci. Eng. 8 (3), 865–879.
Wang, C., Jiang, Y., Liu, R., Wang, C., Zhang, Z., Sugimoto, S., 2020b. Experimental study of the nonlinear flow characteristics of fluid in 3D rough-walled fractures during shear process. Rock Mech. Rock Eng. 53 (6), 2581–2604.
Wittke, W., 1990. Rock Mechanics: Theory and Applications-With Case Histories. Springer-Verlag, Berlin, Heidelberg. New York, London.
Xiong, F., Jiang, Q., Ye, Z., Zhang, X., 2018. Nonlinear flow behavior through rough-walled rock fractures: the effect of contact area. Comput. Geotech. 102, 179–195.
Yin, Q., Ma, G., Jing, H., Wang, H., Su, H., Wang, Y., Liu, R., 2017. Hydraulic properties of 3D rough-walled fractures during shearing: an experimental study. J. Hydrol. 555, 169–184.
Yu, L., Liu, R., Jiang, Y., 2017. A review of critical conditions for the onset of nonlinear fluid flow in rock fractures. Geofluids 1–17, 2017.
Zeng, Z., Grigg, R., 2006. A criterion for non-Darcy flow in porous media. Transport Porous Media 63 (1), 57–69.
Zhang, Z., Nemcik, J., 2013. Fluid flow regimes and nonlinear flow characteristics in deformable rock fractures. J. Hydrol. 477, 139–151.
Zhou, J., Hu, S., Fang, S., Chen, Y., Zhou, C., 2015. Nonlinear flow behavior at low Reynolds numbers through rough-walled fractures subjected to normal compressive loading. Int. J. Rock Mech. Min. Sci. 80, 202–218.
Zhou, J., Wang, M., Wang, L., Chen, Y., Zhou, C., 2018. Emergence of nonlinear laminar flow in fractures during shear. Rock Mech. Rock Eng. 51 (11), 3635–3643.
Zimmerman, R.W., Bodvarsson, G.S., 1996. Hydraulic conductivity of rock fractures. Transport Porous Media 23 (1), 1–30.
Zimmerman, R.W., Al-Yaarubi, A., Pain, C.C., Grattoni, C.A., 2004. Non-linear regimes of fluid flow in rock fractures. Int. J. Rock Mech. Min. Sci. 41, 163–169.
Zou, L., Jing, L., Cvetkovic, V., 2015. Roughness decomposition and nonlinear fluid flow in a single rock fracture. Int. J. Rock Mech. Min. Sci. 75, 102–118.
Zou, L., Jing, L., Cvetkovic, V., 2017. Shear-enhanced nonlinear flow in rough-walled rock fractures. Int. J. Rock Mech. Min. Sci. 97, 33–45.

Yujing Jiang is an academician in Engineering Academy of Japan. He obtained his BSc and MSc degrees from Shandong University of Science and Technology (SDUST), China, in 1982 and 1985, respectively, and his PhD from Kyushu University, Japan, in 1993. He is currently the director of the State Key Laboratory of Mining Disaster Prevention and Control Co-founded by Shandong Province and the Ministry of Science and Technology, vice chairman of the Soft-rock Engineering and Deep Disaster Control Sub-society of Chinese Society for Rock Mechanics and Engineering (CSRME). He is also winner of Joint Research Fund for Overseas Natural Science of China. His main research interests include (1) environmental geotechnical engineering, (2) rock mechanics and rock engineering, (3) development and utilization of underground space, (4) remote monitoring forecast and control for geological disaster, (5) mining of deep-sea resources (natural gas hydrate) and control of seabed strata environment, and (6) mine pressure and strata control. He has published 15 books in Chinese and foreign languages and over 300 research papers. He is vice editor of *Rock Mechanics and Rock Engineering*, and also serves as the editorial board member of several journals, including *Journal of Rock Mechanics and Geotechnical Engineering* (JRMGE).